Materials Transactions, Vol. 45, No. 7 (2004) pp. 2128 to 2136
Special Issue on Grain Boundaries, Interfaces, Defects and Localized Quantum Structures in Ceramics

Improvement of Oxidation Resistance and Oxidation-Induced Embrittlement by Controlling Grain Boundary Microstructure in Silicon Carbides with Different Dopants

Sadahiro Tsurekawa[1,*1], Hiroaki Watanabe[1,*2], Nobuyuki Tamari[2] and Tadao Watanabe[1]

[1]*Laboratory of Materials Design and Interface Engineering, Department of Nanomechanics, Graduate School of Engineering, Tohoku University, Sendai 980-8579, Japan*
[2]*Kansai Center, National Institute of Advanced Industrial Science and Technology, Ikeda 563-8577, Japan*

High temperature oxidation and oxidation-induced embrittlement in β-silicon carbides (SiCs) with different grain boundary microstructures have been studied. SiCs with different grain boundary microstructures were fabricated by hot-pressing with different doping elements like Mg, Al, P. Oxidation experiments were carried out under the oxygen partial pressure ranging from 0.303 Pa to 78.5 Pa at temperatures 1623–1773 K for 7.2–36 ks. Thereafter, the degree of oxidation-induced embrittlement was quantitatively evaluated by three-point bend tests at room temperature in connection with grain boundary microstructure. More severe degradation was observed as a result of oxidation though the passive oxidation took place. It is concluded that the oxidation-induced embrittlement in β-SiC can be improved by decreasing the frequency of random boundaries and the grain size. The potential of grain boundary engineering for a ceramic material has been confirmed.

(Received February 16, 2004; Accepted March 15, 2004)

Keywords: *silicon carbide, grain boundary, grain boundary character distribution, grain boundary engineering, high-temperature oxidation, oxidation embrittlement, intergranular fracture*

1. Introduction

When polycrystalline materials are exposed to a corrosive and/or an oxidizing atmosphere, corrosion or oxidation preferentially takes place at grain boundaries. Since these degraded boundaries can act as preferential sites for crack initiation and a path of crack propagation, oxidized (corroded) materials often show severe embrittleness, and the embrittlement leads to the premature failure of a machine and structure. From the practical point of view, the phenomena of oxidation and corrosion cause serious problems because the brittle failure due to intergranular degradation often occurs unexpectedly without any clear indication.

To date, a large number of studies were conducted on high temperature intergranular oxidation in metallic materials.[1–8] Brumm *et al.* pointed out that intergranular oxidation occurred preferentially at certain grain boundaries in Ni-Al alloy.[9] According to our recent study on intergranular oxidation in Ni-40 at%Fe alloy,[10] there was a significant difference of the propensity to intergranular oxidation among different types of grain boundaries; random grain boundaries acted as preferential sites for oxidation, while low-Σ CSL boundaries, particularly $\Sigma3$, $\Sigma11$, $\Sigma19$ and $\Sigma27$ CSL boundaries, were immune from oxidation. Furthermore, we have demonstrated that oxidation-induced intergranular embrittlement in Ni-40 at%Fe alloy can be improved by controlling the grain size, the grain boundary character distribution (GBCD) and grain boundary connectivity.[11,12]

In the present study, we have focused on oxidation-induced embrittlement in silicon carbide (SiC) in order to compare with that in metallic materials. Since non-oxide silicon carbide has been expected as a structural material under severe environments such as nuclear fusion reactor and aerospace systems, oxidation behaviour of silicon carbides at high temperatures has been extensively studied so far.[13–23] At higher oxygen partial pressure, such as the level of air, silicon carbide possesses good oxidation resistance at high temperatures because of protective SiO_2 thin film formed on the surface. The "passive oxidation" occurs by the reaction:

$$SiC(s) + \frac{3}{2}O_2(g) = SiO_2(s) + CO(g). \quad (1)$$

However, at certain conditions of low oxygen partial pressure and high temperature, severe "active oxidation" occurs due to the formation of gaseous SiO by the reaction,

$$SiC(s) + O_2(g) = SiO(g) + CO(g). \quad (2)$$

Moreover, the active oxidation causes severe grain boundary attack, resulting in strength degradation and severe brittleness.[21]

Vaughn and Maahs[20] and Narushima *et al.*[23] depicted "oxidation diagram" which presents the active-to-passive oxidation transition for silicon carbides. According to the "oxidation diagram", the transition depends not only oxygen partial pressure and temperature but very likely depends on materials processing. This suggests that the grain boundary microstructure, such as the grain size and the GBCD, can affect oxidation behaviour of silicon carbide. Accordingly, the design and control of grain boundary microstructure may have a potential of enhancement of oxidation resistance in non-oxidation ceramics.

In the case of metallic materials, grain boundary microstructure can be controlled by the thermomechanical treatments.[24] However, this is not a case of ceramics where the application of the thermomechanical treatment is difficult because of their lack of workability. We have paid our particular attention to the potency of dopant in controlling grain boundary microstructure, because the stacking fault

*1Corresponding author, E-mail: turekawa@mdie.mech.tohoku.ac.jp
*2Graduate Student, Tohoku University

Table 1 Chemical composition of β-SiC powder used in this work.

Element	C (mass%)	O (mass%)	N (ppm)	Ca (ppm)	K (ppm)	Fe (ppm)	Cr (ppm)	Ni (ppm)	Al (ppm)	Na (ppm)	Zn (ppm)
Contents	32.20	0.472	0.018	0.1	ND	ND	ND	ND	ND	0.1	ND

ND: not detected

energy of silicon carbide can change depending on the kind of sintering aids.[25,26] To our knowledge, however, there have been few investigations into the effect of doping element on the grain boundary microstructure, particularly on the GBCD, in silicon carbide.

In the course of this work, we have studied the effects of different doping elements on the grain boundary microstructure, oxidation behaviour and fracture stress in β-silicon carbides. The observed changes in the fracture strength caused by oxidation were examined in connection with the grain boundary microstructure. On the basis of present observations, we will discuss the optimal grain boundary microstructure for suppressing oxidation-induced intergranular embrittlement in silicon carbide, and show the potential of grain boundary engineering for development of high performance ceramic materials through controlling the GBCD.

2. Experimental Procedures

2.1 Sample preparation

Ultra high-purity β-SiC powder (Sumitomo Osaka Cement Co., Ltd.), with the average particle size of 0.03 μm, was used as a starting material. Chemical composition of the powder was shown in Table 1. Magnesium, aluminum and phosphor, which are on the same period but possess different valence in the periodic table, were selected as doping elements; 0.5 mass% Mg, 0.2 mass% Al or 0.5 mass% P was doped into raw β-SiC powder together with sintering aid of 0.5 mass% B. Those ingredients were milled in ethanol with SiC balls for 24 h. After drying, they were hot-pressed at 2373 K for 300 s under 40 MPa in air, and resulted in ca. 99% theoretical density. The residual contents of doping elements were 0.16, 0.15 and 0.05 mass% for Mg, Al and P, respectively after sintering.

We observed the grain boundary structures by high resolution electron microscopy (HRTEM) and analyzed chemical compositions using the energy dispersive X-ray spectrometry (EDS) with an ultra-thin window attached to a HITACHI HF-2000 FEG-TEM. HRTEM studies indicated that doping elements like Al and Mg did not form a second phase along the grain boundaries. However, FEG-TEM/EDS analyses revealed that doping elements partly segregated to grain boundaries.[27] An X-ray diffractometer was applied to detected any change in polytype composition in hot-pressed SiC samples using Ruska's method,[28] and the obtained results are shown in Table 2. We found that there was a slightly difference in the fraction of polytype among them; the fraction of β phase (3C structure) in undoped and Al-doped SiCs was 88%, while the fraction in Mg- and P-doped SiCs was 98%.

2.2 Evaluation of grain boundary microstructure

Orientation imaging microscopy (OIM) was applied to quantitative evaluation of the grain boundary microstructures such as the grain orientation distribution and the grain boundary character distribution (GBCD) with a HITACHI S-4200 cold FEG-SEM equipped with TSL OIM system, which provided a resolution power of less than 50 nm in the OIM mode. The FEG-SEM was worked at an accelerating voltage of 30 kV and a beam current of 14 μA. The electron beam was scanned on the specimen surface at regular hexagonal grid of 100 nm step size.

Table 2 Percentage of polytype in HPed silicon carbides.

Specimen	Polytype (%)			
	β-SiC	α-SiC		
	3C	4H	6H	15R
SiC (undoped)	88	3	7	2
SiC (Mg-doped)	98	0	2	0
SiC (Al-doped)	88	1	9	2
SiC (P-doped)	98	0	2	0

The samples suitable for OIM analysis were mechanically polished to a mirror surface and buff-finished with colloidal silica of 0.04 μm in particle size. Thereafter, the specimen surface was chemically etched in the Murakami etcher ($K_3[Fe(CN)_6]$ 10 g + NaOH 10 g + distilled water 100 ml) to remove residual surface strain probably introduced by the mechanical polishing.

2.3 Oxidation experiment and evaluation of oxidation embrittlement

Oxidation tests were carried out in a resistance heat furnace under the partial pressure of oxygen, P_{O_2} ranging 0.303–78.5 Pa at temperatures 1623–1773 K for 7.2–36 ks. The oxygen partial pressure was controlled by using a mixed gas with O_2 + Ar. These oxidation conditions were chosen referring to the "oxidation diagram" by Vaughn and Maahs[20] to cover both active and passive oxidation regions. A sample for the oxidation test was designed as 17 mm × 2 mm × 1 mm in dimensions, which was suitable for the following three-point bend fracture test. After oxidation test, the mass change was measured using an electronic balance with a sensitivity of 1 μg, and the surface morphology was observed by FEG-SEM. The oxidation-induced embrittlement was evaluated by the three-point bend fracture test at room temperature, and the results were discussed in connection with the grain boundary microstructure.

3. Results and Discussion

3.1 Effect of dopant on grain boundary microstructure

Figure 1 shows the SEM micrographs of β-SiC samples sintered with different doping elements. These micrographs reveal that the doping elements exert a strong influence on the grain size but little on the aspect ratio of grains. The

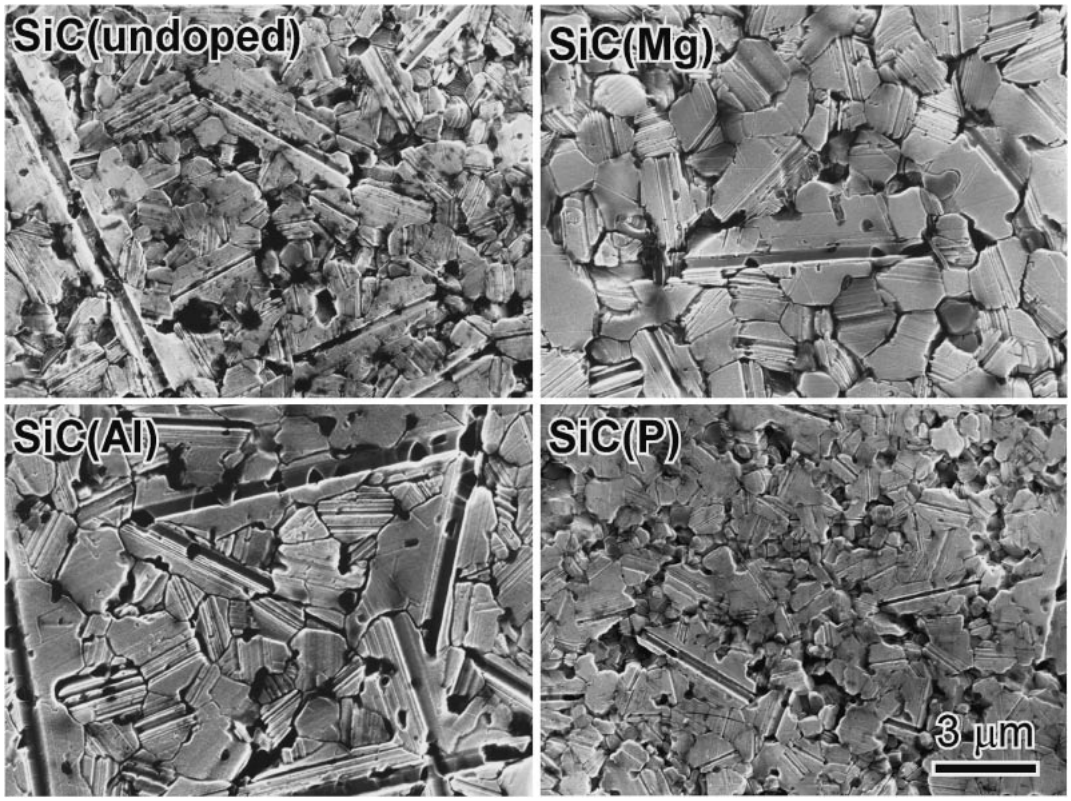

Fig. 1 SEM micrographs of hot-pressed β-SiC samples with different doping elements.

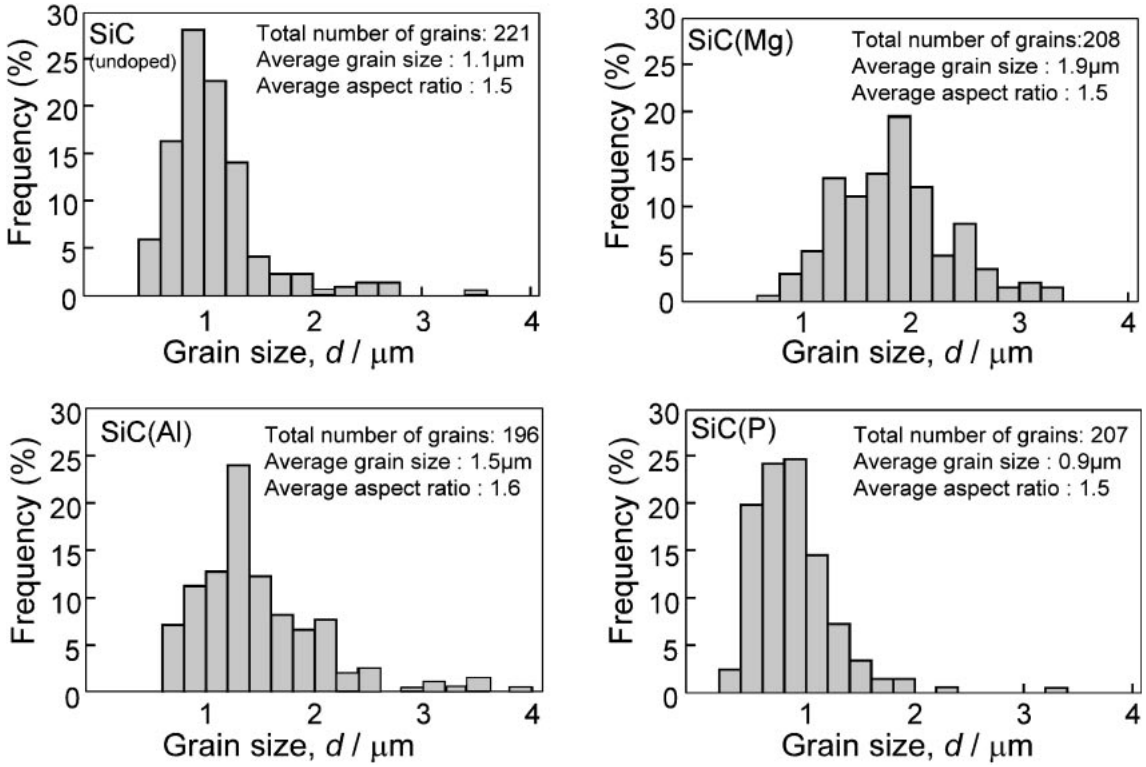

Fig. 2 Grain size distributions in β-SiC samples with different doping elements. The average grain size and aspect ratio are shown in each histogram.

histograms for the grain size distributions in these samples are shown in Fig. 2. The average grain size and the aspect ratio are also given. The average grain size depends on the doping elements; 1.9 μm, 1.5 μm and 0.9 μm for Mg-, Al- and P-doped SiCs, respectively, and 1.1 μm for undoped SiC. Silicon carbide partially possesses ionic character of bonding as well as covalent bonding. Assuming that the doped elements substitutionally occupy the Si atom sites (that is,

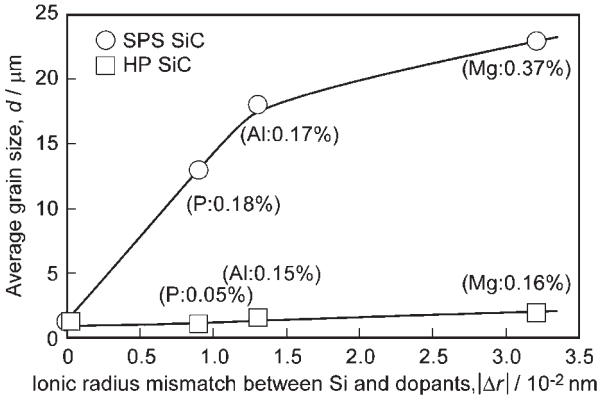

Fig. 3 Effect of ionic radius mismatch between Si and doping elements on the average grain size in hot-pressed β-SiC samples and spark plasma sintered β-SiC samples.

doped elements possess 4-fold coordination), the differences in the ionic radius between dopants and Si are 0.032, 0.013 and 0.009 nm for Mg, Al and P, respectively. The average grain sizes were exhibited as a function of the ionic radius mismatch in Fig. 3. For comparison, the data obtained from spark plasma sintered (SPS) β-SiCs[29] are also shown in Fig. 3. Although the residual quantity of doping elements was different among these samples, the larger the ionic radius mismatch, the more significantly grain growth rate increased in hot-pressed and SPS samples. The effect of doping elements on grain growth in SiC may becomes significant as the ionic radius mismatch between Si and doping element increases, though further study should be required to confirm the assumption.

Figure 4 shows the grain boundary character distribution obtained from the OIM analyses for β-SiC samples with different doping elements. As previously expected, the grain boundary character distribution could be controlled by selecting doping elements. In particular, the frequency of $\Sigma 3$ boundary widely changed ranging from 15 to 25%, while the frequency of CSL boundaries except $\Sigma 3$ boundary was similar to that estimated from the random polycrystal irrespective of doping elements.[30] Conversely, the frequencies of the random boundaries, which would be preferentially oxidized, were approximately 65% in undoped and Al-doped SiCs, and 71% in Mg- and P-doped SiC samples. The observed doping effect on grain boundary microstructure was discussed in detail in the previous paper.[27]

3.2 Oxidation behavior

3.2.1 Oxidation time dependence

Figure 5 shows the specific mass changes due to oxidation for SiC samples with different doping elements kept in an oxygen partial pressure of 78.5 Pa at 1773 K. The specific mass of the oxidized samples was found to increase parabolically with increasing oxidation time, indicating that the passive oxidation occurred irrespective of doping elements. However, it is evident that the oxidation rates were different depending on doping elements. In particular, Mg doping remarkably enhanced oxidation. The oxidation rate of Mg-doped SiC was approximately one order higher than that of undoped SiC under the condition described above.

The square of the specific mass gain is plotted as a function of oxidation time in Figs. 6(a) and (b). The parabolic rate constants, k_p, calculated from the specific mass gain are 8.4×10^{-3} mg^2/(cm^4·h), 4.3×10^{-4} mg^2/(cm^4·h), 6.5×10^{-5} mg^2/(cm^4·h) and 8.5×10^{-5} mg^2/(cm^4·h) for Mg-, Al-, P-doped SiC samples and undoped one, respectively. With the

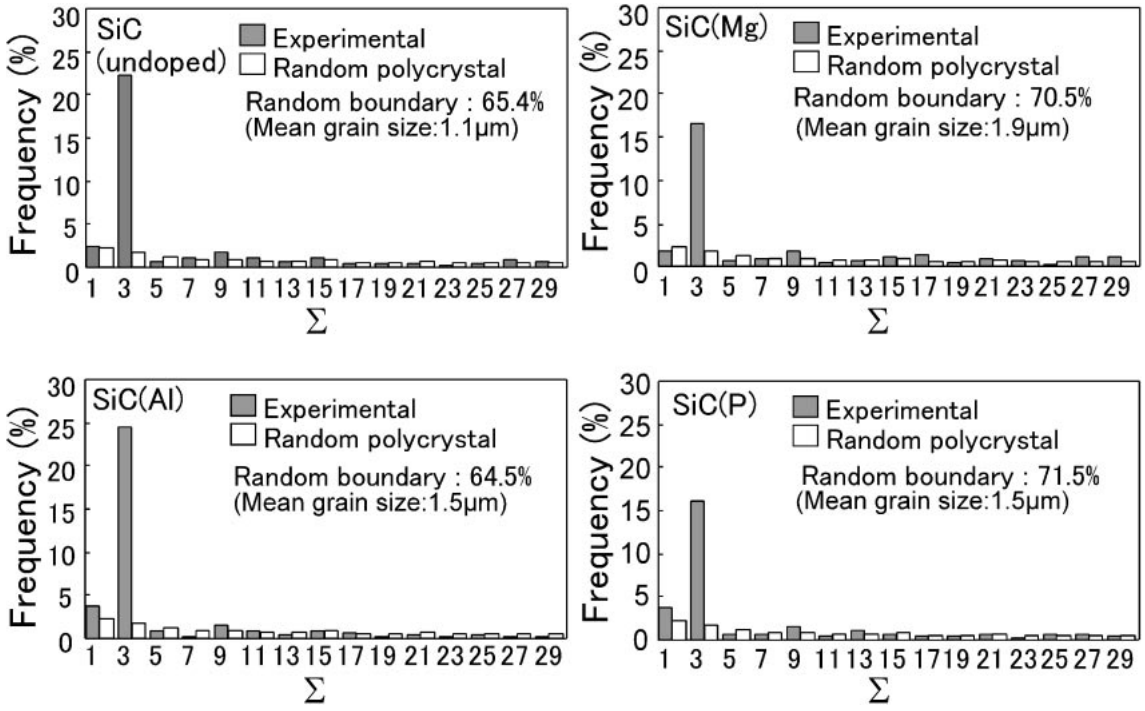

Fig. 4 Grain boundary character distribution (GBCD) in SiC samples with different dopants. The frequency of Σ3 boundaries can be widely changed ranging 15% to 25% by selecting a doping element.

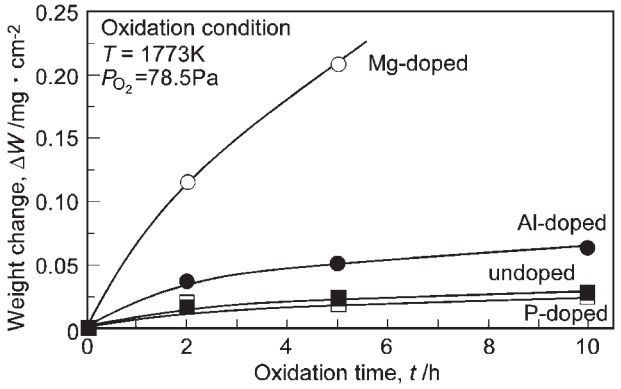

Fig. 5 Weight change as a function of time for different β-SiC samples oxidized at an oxygen partial pressure of 78.5 Pa and at 1773 K.

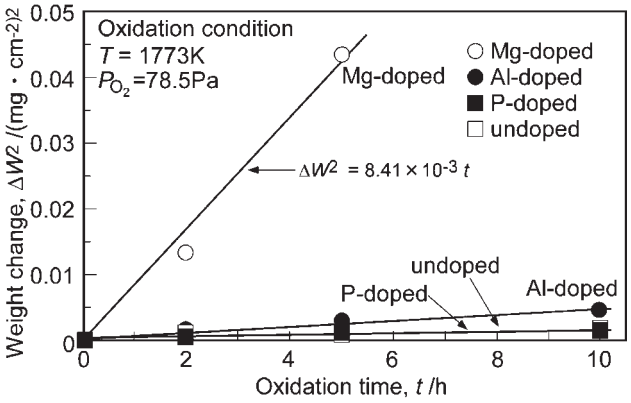

(a)

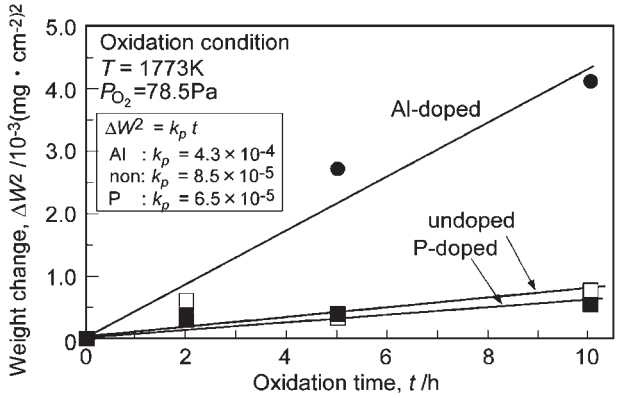

(b)

Fig. 6 Parabolic plot of oxidation behavior of different β-SiC samples at an oxygen partial pressure of 78.5 Pa and at 1773 K (a). Figure (b) shows an enlarged figure of oxidation behavior for Al-, P-doped and undoped β-SiC samples. The parabolic rate constants for each sample are shown in the figures.

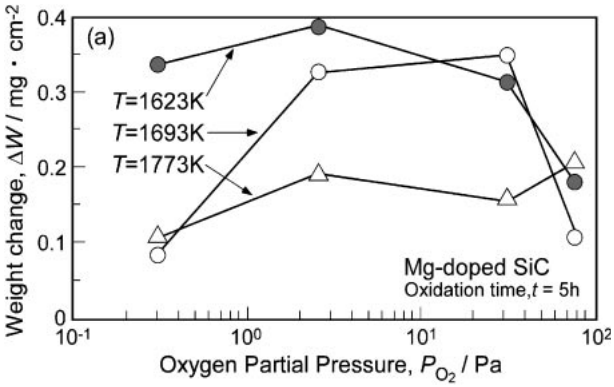

(a)

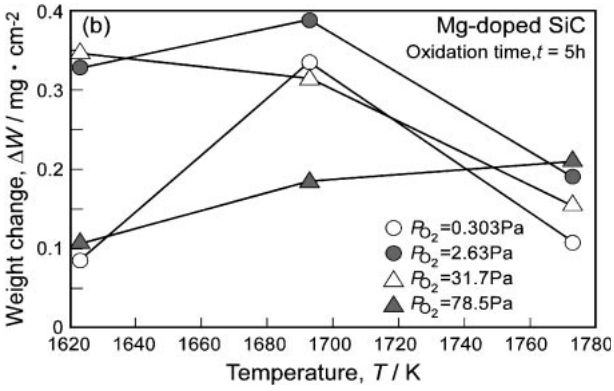

(b)

Fig. 7 Oxygen partial pressure dependence of weight change (specific mass gain) for Mg-doped β-SiC oxidized at different temperatures for 5 hours (a), and temperature-dependence of weight changes at different oxygen partial pressures (b).

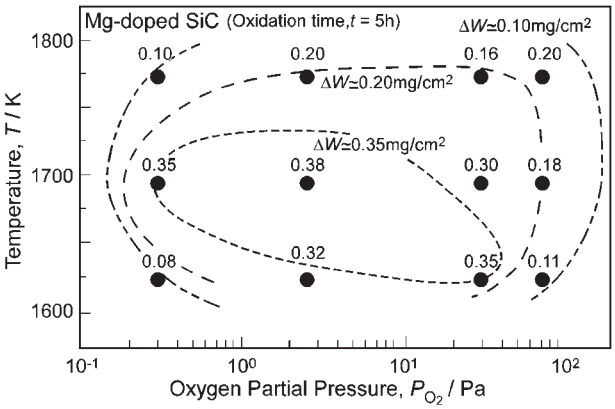

Fig. 8 The oxidation diagram for Mg-doped β-SiC. The numerals in the figure indicate the specific mass gain during oxidation for 5 hours, given in the unit of mg/cm^2.

reference of the literature data,[14,17,22,23] these obtained values are 1–2 order magnitude lower than those for hot-pressed SiC samples but similar to those for CVD SiC in dry oxygen atmosphere.

3.2.2 Effects of temperature and oxygen partial pressure

Figures 7(a) and (b) show the effects of oxygen partial pressure and temperature on the specific mass gain of Mg-doped SiC, respectively. Figure 7 revels that the specific mass gain of Mg-doped SiC significantly changes not only with the oxygen partial pressure but also with temperature. Moreover, there appears a peak in the mass gain at a certain oxygen partial pressure at 1623 K and 1693 K, whereas the mass gain increases with increasing the oxygen partial pressure at 1773 K.

Figure 8 present a "oxidation diagram" for Mg-doped SiC, showing the effects of temperature and the oxygen partial

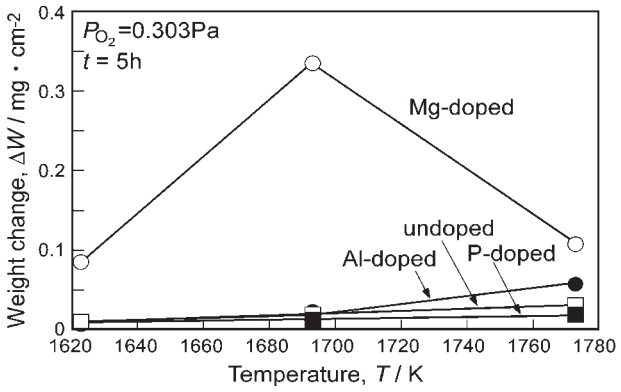

Fig. 9 Temperature-dependence of weight changes (specific mass gain) for Mg-, Al-, P-doped and undoped β-SiCs oxidized at an oxygen partial pressure of 0.303 Pa for 5 hours.

pressure on the specific mass gain. The numeral shown in Fig. 8 represent the specific mass gain in the unit of mg/cm^2 after oxidation under given condition. We can see that the specific mass gain significantly changes depending on the oxygen partial pressure and temperature. There is a peak in the mass gain around 1700 K and 3 Pa in oxygen partial pressure, that is oxidation of Mg-doped SiC is the most severe in this conditions.

On the other hand, the specific mass gain for Al-doped SiC was found to increase with increasing temperature as shown in Fig. 9, while notable change was not observed for P-doped and undoped SiC samples. Figure 10 exhibits the influence of oxygen partial pressure on the specific mass gain for Al-, P-doped and undoped SiC samples at different temperatures. Similar dependence of the mass gain on oxygen partial pressure was observed between these samples and Mg-doped SiC. The mass gain was maximized at a certain oxygen partial pressure at 1623 K and 1693 K but kept increasing with increasing the oxygen partial pressure at 1773 K The oxygen partial pressure produced the maximum mass gain was found to increase with increasing temperature.

3.2.3 Observation of oxidized surface morphology

The morphology of oxidized SiC surfaces was observed by SEM. As shown in Fig. 11, SEM micrographs reveal that dense and smooth oxide film was formed on the surface of P-doped and undoped SiC samples. The X-ray diffraction measurement with a diffractometer gave qualitative analysis of the surface oxide film. A small peak in X-ray spectrum corresponding to crystalline SiO_2 (cristobalite) was observed irrespective of doping elements. In addition, small amounts of mullite was present in the case of Al-doped SiC. Hence, crystallization from glass SiO_2 to cristobalite occurred in the surface oxide film to some extent. On the other hand, the surface SiO_2 film on the Al- and Mg-doped SiC samples was partially broken probably due to the formation of gas bubbles at the SiC/SiO_2 interface. Mg-doping especially promoted gas bubbling, so that the SiO_2 film of Mg-doped SiC was observed just like a crater, where extensive grain boundary attack occurred as shown in Fig. 11.

Singhal[14] reported that impurity elements like Al, K were present in much greater quantities in the oxide film than in the SiC substrate. Since the presence of doping element like Al

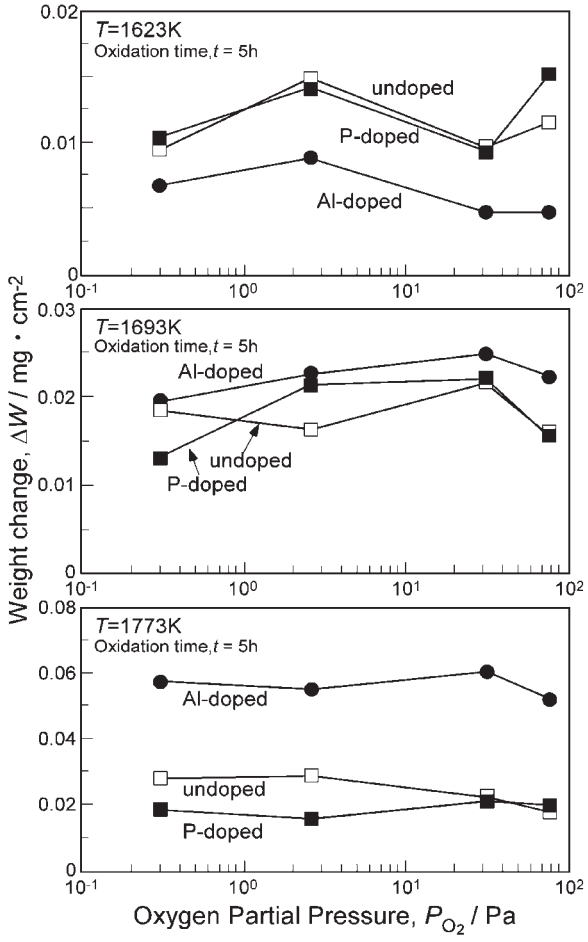

Fig. 10 Oxygen partial pressure dependence of weight changes for Al-, P-doped and undoped β-SiC samples oxidized at different temperatures for 5 hours.

and Mg in oxide film can cause rapid decrease in melting temperature of SiO_2 (cristobalite), the rate of oxygen diffusion in impure SiO_2 surface film should increase. Accordingly, the rate of oxidation could increase by doping of Mg and Al. Alternatively, Mg atoms are known to act as "network modifiers" in glass SiO_2; that is, Mg atoms break tetrahedrally bonded Si-O network, whereas Al and P atoms act as "network former".[31] Since this breakdown of Si-O bond network generally yields a decrease in the viscosity of glass phase, the gaseous diffusion in SiO_2 film increases in accordance with Storks-Einstein relation.

Taking those observations and discussion together, it is clear that the inward diffusion of O_2 in SiO_2 film may be faster than the outward diffusion of CO gas for Mg- or Al-doped SiC samples, so that CO gas accumulate at SiC/SiO_2 interface and form SiO_2 bubble.

3.3 Evaluation of oxidation embrittlement

After oxidation tests, the samples were subjected to the three-point bend fracture tests at room temperature to evaluate oxidation-induced embrittlement. Figures 12(a) and (b) show stress-strain curves at room temperature before and after oxidation, respectively. The specimens shown in Fig. 12(b) were oxidized under an oxygen partial pressure of 78.5 Pa at 1773 K for 18 ks (5 h). It is found that there was less

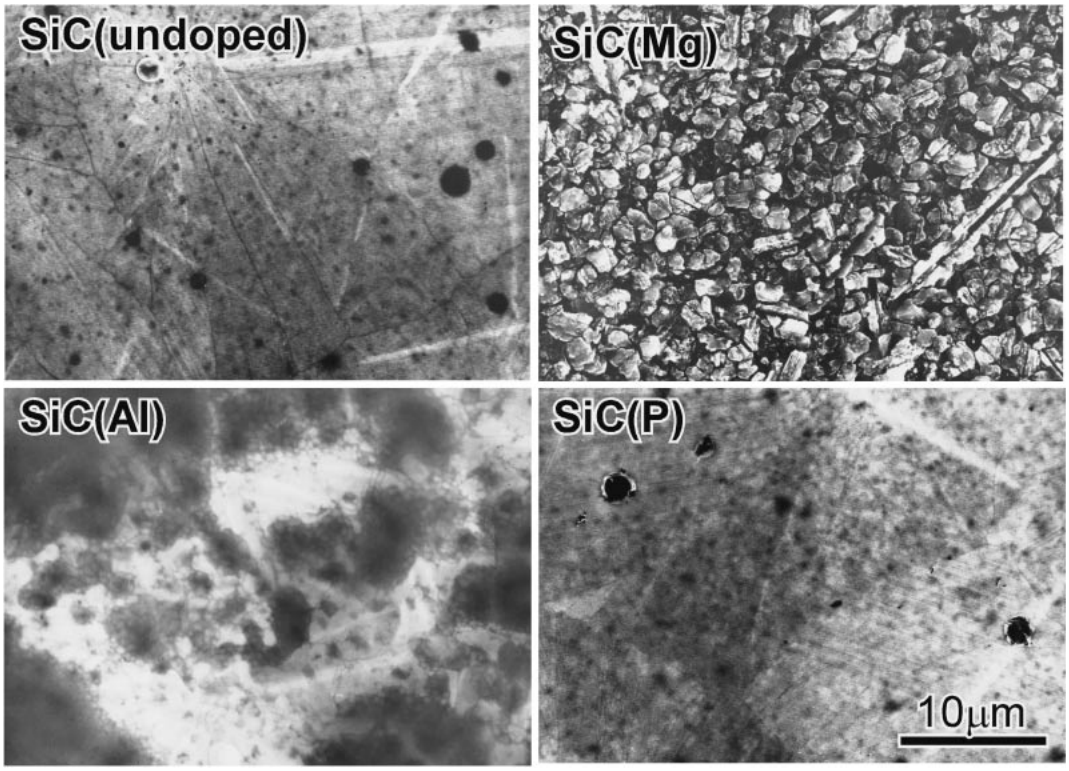

Fig. 11 SEM micrographs showing surface morphology for undoped and doped SiC samples after oxidation test.

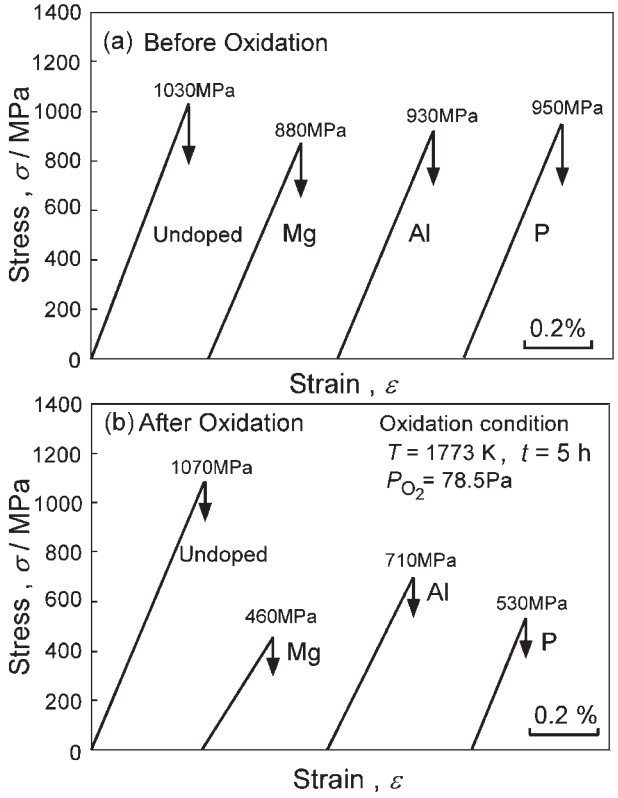

Fig. 12 Stress-strain curves for β-SiC with different dopants: (a) before oxidation and (b) after oxidation. The oxidation conditions are shown in the figure.

difference in the fracture stress among these SiC samples before oxidation, ranging from 900 to 1000 MPa. However, we can recognize that the fracture stress increases with decreasing the average grain size. On the other hand, a remarkable strength degradation was observed in Mg-, Al- and P-doped SiC samples due to oxidation even when the passive oxidation had taken place. In particular, an approximately 50% reduction in the fracture stress was observed in Mg-doped SiC in which the specific mass gain was the largest among the samples. Nevertheless, there was little change in the fracture stress for undoped SiC after oxidation.

Figure 13 demonstrates the fracture surface morphology in doped and undoped SiC samples after oxidation and bend fracture tests. These SEM micrographs reveal that the transgranular fracture was predominant in Al-doped and undoped SiC samples, whereas pronounced intergranular fracture occurred in Mg-doped SiC which showed the most severe oxidation embrittlement. Also, intergranular fracture morphology was somewhat observed in P-doped SiC. Accordingly, it is supposed that the intergranular oxidation is responsible for the remarkable strength degradation in SiC.

From these results, we must emphasize that the passive oxidation is not always protect the material against oxidation-induced embrittlement. Oxygen is supplied by diffusion through SiO_2 film in SiC, then the intergranular oxidation is likely to proceed below the oxide film. In addition, breakdown of surface SiO_2 film due to CO gas bubbling at SiC/SiO_2 interface enhances intergranular attack in substrate.

3.4 The control of oxidation embrittlement by grain boundary engineering

We have examined the relationship between the oxidation-induced embrittlement in SiC and the grain boundary microstructure, and the potential of grain boundary engineering for the material. Figure 14 represents the effects of the

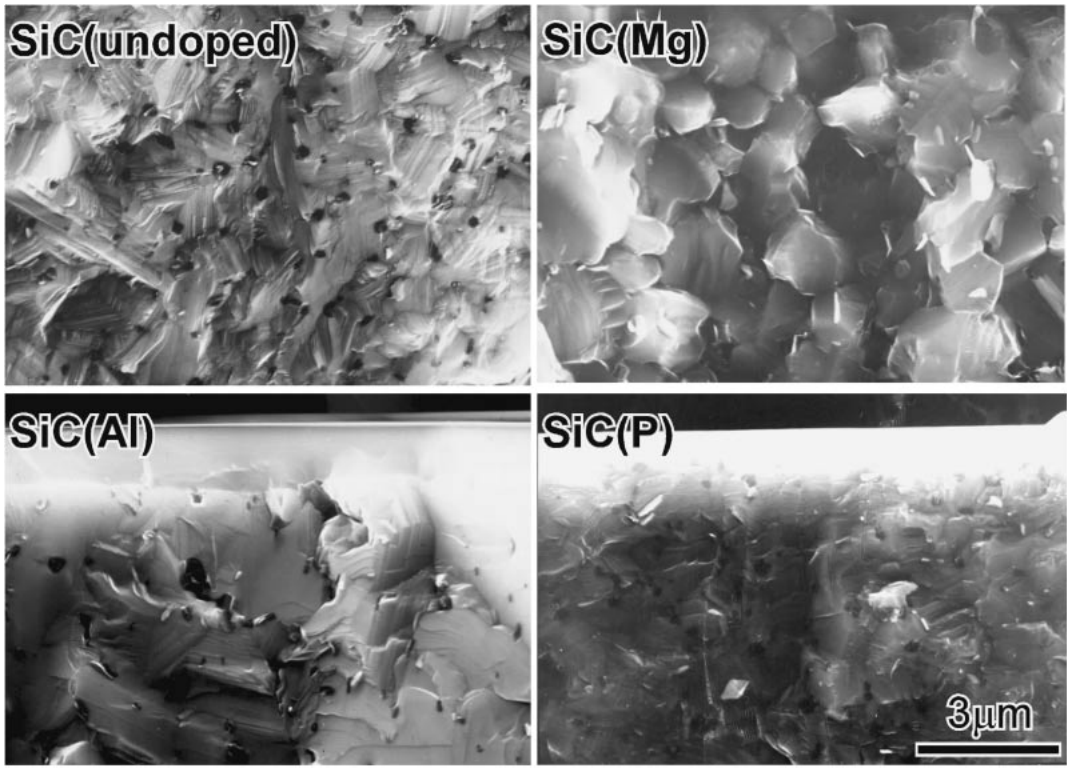

Fig. 13 SEM micrographs showing fracture surface morphology for oxidized β-SiC samples with different dopants.

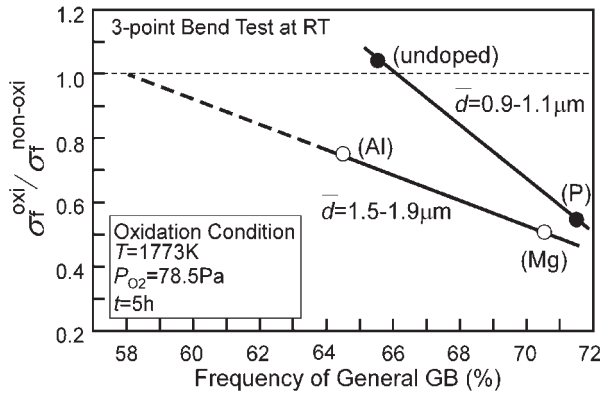

Fig. 14 Oxidation-induced embrittlement depending on the frequency of random boundaries and the grain size.

GBCD and the grain size on oxidation-induced embrittlement in SiC. The fracture stresses of oxidized samples were normalized by the stresses before oxidation, and plotted against the frequency of random boundaries (*i.e.*, against the GBCD). The more severe oxidation-induced embrittlement occurs, the lower the value of $\sigma_f^{oxi}/\sigma_f^{non\text{-}oxi}$ was obtained. The data in Fig. 14 can be classified into two groups depending on the grain size. It is evident that the strength degradation due to the oxidation increases with increasing the frequency of random boundaries and with increasing the grain size. In addition, the GBCD dependence of the stress degradation appears of much significance as the grain size increases. The results mentioned above are in good agreement with the results concerning the oxidation-induced embrittlement in a Ni-40 at%Fe alloy.[11,12] Since the intergranular oxidation takes place preferentially at random boundaries,[10] a decrease in the fraction of random boundaries, conversely an increase in the fraction of coincidence boundaries, is essential to the control of oxidation-induced embrittlement. For the intergranular oxidation likely proceeds as a percolation process, the connectivity of random grain boundary is of great importance as well as the GBCD. If the crack propagating along the oxidized random boundaries meets a coincidence boundary with a higher resistance for fracture at a triple junction, the crack propagation could be prevented from further propagation. According to the percolation theory, the percolation threshold in bond process in two-dimensional hexagonal cluster is 0.65.[32] Therefore, the frequency of random boundaries which are preferential sites for oxidation and fracture should be lower below about 50%–65% in order to prevent propagation of intergranular cracks along random boundaries less connecting to each other.

4. Conclusions

Particular attentions have been paid for high temperature oxidation behavior and oxidation-induced embrittlement in grain boundary engineered silicon carbide by doping. The main results obtained are as follows:

(1) The grain boundary microstructure defined by the grain size and the grain boundary character distribution (GBCD) could be successfully controlled by doping of different kinds of elements (Mg, Al and P). In particular, the frequency of $\Sigma 3$ boundaries widely changed ranging from 15 to 25%.

(2) The grain growth rate could be more enhanced depending on the difference in the ionic radius between silicon

and doping elements increased (Mg>Al>P).

(3) Passive oxidation was observed under any conditions irrespective of dopants. In particular, the oxidation in Mg-doped SiC was remarkably enhanced and the specific mass gain was approximately one order higher in Mg-doped SiC than in undoped SiC.

(4) A remarkable strength degradation was observed in Mg-, Al- and P-doped SiC samples due to oxidation even though the passive oxidation took place. We have found that the strength degradation can be improved by decreasing the frequency of random boundaries and the grain size. From this work, the potential of the grain boundary engineering for non-oxide ceramic SiC materials was confirmed.

Acknowledgements

The authors would like to express their sincere thanks to Mr. T. Matsuzaki (Tohoku University) for his help in experiments for oxidation tests. This work was supported by a Grant-in-Aid for Basic Research (B)(12450277) and for COE Research from the Ministry of Education, Science, Sports and Culture of Japan.

REFERENCES

1) F. Matsuno, S. Nishikida and T. Harada: Tetsu to Hagane **67** (1981) 2029–2038.
2) R. H. Bricknell and D. A. Woodford: Metall. Trans. **12A** (1981) 425–433.
3) D. A. Woodford and R. H. Bricknell: Metall. Trans. **12A** (1981) 1467–1475.
4) R. H. Bricknell and D. A. Woodford: Metall. Trans. **12A** (1981) 1673–1680.
5) Y. Shida, F. H. Stott, B. D. Bastow, D. P. Whittle and G. C. Wood: Oxid. Metal. **18** (1982) 93–113.
6) Z. Rizhang, G. Manjiou and Z. Yu: Oxid. Metal. **27** (1987) 253.
7) K. Kusabiraki, H. Toki, T. Ishiguro and T. Ooka: Tetsu to Hagane **74** (1988) 871–878.
8) K. Kusabiraki, J. Ikegami, T. Nishimoto and T. Ooka: Tetsu to Hagane **80** (1994) 82–87.
9) M. W. Brumm, H. J. Grabke and B. Wagemann: Corros. Sci. **36** (1994) 37–53.
10) S. Yamaura, Y. Igarashi, S. Tsurekawa and T. Watanabe: Acta Mater. **47** (1999) 1163–1174.
11) S. Yamaura, Y. Igarashi, S. Tsurekawa and T. Watanabe: *Properties of Complex Inorganic Solids 2*, (Kluwer Academic/Plenum Publishers, 2000) 27–37.
12) S. Yamaura, S. Tsurekawa and T. Watanabe: Mater. Trans. **44** (2003) 1494–1502.
13) S. C. Singhal and F. F. Lange: J. Am. Ceram. Soc. **58** (1975) 433–435.
14) S. C. Singhal: J. Mater. Sci. **11** (1976) 1246–1253.
15) J. A. Costello and R. E. Tressler: J. Am. Ceram. Soc. **64** (1981) 327–331.
16) J. A. Costello, R. E. Tressler and I. S. T. Tsong: J. Am. Ceram. Soc. **64** (1981) 332–335.
17) J. A. Costello and R. E. Tressler: J. Am. Ceram. Soc. **69** (1986) 674–681.
18) J. L. Smialek and N. S. Jacobson: J. Am. Ceram. Soc. **69** (1986) 741–752.
19) M. Maeda, K. Nakamura and M. Yamada: J. Am. Ceram. Soc. **72** (1989) 512–514.
20) W. L. Vaughn and H. G. Maahs: J. Am. Ceram. Soc. **73** (1990) 1540–1543.
21) H. E. Kim and A. J. Moorhead: J. Am. Ceram. Soc. **73** (1990) 1868–1872.
22) J. W. Fergus and W. L. Worrell: J. Am. Ceram. Soc. **78** (1995) 1961–1964.
23) T. Narushima, T. Goto, T. Hirai and Y. Iguchi: Mater. Trans., JIM **38** (1997) 821–835.
24) T. Watanabe: Texture and Microstructure **20** (1993) 195–216.
25) K. Kawahara, S. Tsurekawa and H. Nakashima: Proc. 6th Intern Symp on Ceramic Materials and Components for Engines, (1997) 724–729.
26) K. Kawahara, S. Tsurekawa and H. Nakashima: J. Japan Inst. Metals **62** (1998) 246–254.
27) V. S. R. Murthy, K. Kawahara, S. Tsurekawa, T. Watanabe and N. Tamari: Submitted to J Am Ceram Soc.
28) J. Ruska, L. I. Gauckler, J. Lorenz and H. U. Rexer: J. Mater. Sci. **14** (1979) 2013–2017.
29) S. Tsurekawa, Y. Naito, V. S. R. Murthy, T. Watanabe and N. Tamori: Key Eng. Mater. **247** (2003) 331–334.
30) A. Morawice, J. A. Szpunar and D. C. Hinz: Acta Metall. Mater. **41** (1993) 2825–2832.
31) E. T. Turkdogan and P. M. Bills: Ceram. Bull. **39** (1960) 682–687.
32) T. Odagaki: *Introduction to Percolation Physics*, (Shokabo, 1993).